Front. Mater. Sci. 2024, 18(2): 240685
https://doi.org/10.1007/s11706-024-0685-9

RESEARCH ARTICLE

High-stability double-layer polymer–inorganic composite electrolyte fabricated through ultraviolet curing process for solid-state lithium metal batteries

Xinghua Liang[1*], Pengcheng Shen[1*], Lingxiao Lan[1*], Yunmei Qin (✉)[1], Ge Yan (✉)[2], Meihong Huang[3], Xuanan Lu[1], Qiankun Hun[1], Yujiang Wang[1], and Jixuan Wang[3]

1 Guangxi Key Laboratory of Automobile Components and Vehicle Technology, Guangxi University of Science & Technology, Liuzhou 545006, China
2 Guangxi Automobile Group Co., Ltd., Liuzhou 545006, China
3 School of Automotive Engineering, Guangdong Polytechnic of Industry and Commerce, Guangzhou 510510, China

ABSTRACT: Electrolyte interface resistance and low ionic conductivity are essential issues for commercializing solid-state lithium metal batteries (SSLMBs). This work details the fabrication of a double-layer solid composite electrolyte (DLSCE) for SSLMBs. The composite comprises poly(vinylidene fluoride-*co*-hexafluoropropylene) (PVDF–HFP) and poly(methyl methacrylate) (PMMA) combined with 10 wt.% of $Li_{6.4}La_3Zr_{1.4}Ta_{0.6}O_{12}$ (LLZTO), synthesized through an ultraviolet curing process. The ionic conductivity of the DLSCE (2.6×10^{-4} S·cm^{-1}) at room temperature is the high lithium-ion transference number (0.57), and the tensile strength is 17.8 MPa. When this DLSCE was assembled, the resulted LFP/DLSCE/Li battery exhibited excellent rate performance, with the discharge specific capacities of 162.4, 146.9, 93.6, and 64.0 mA·h·g^{-1} at 0.1, 0.2, 0.5, and 1 C, respectively. Furthermore, the DLSCE demonstrates remarkable stability with lithium metal batteries, facilitating the stable operation of a Li/Li symmetric battery for over 200 h at both 0.1 and 0.2 mA·cm^{-2}. Notably, the formation of lithium dendrites is also effectively inhibited during cycling. This work provides a novel design strategy and preparation method for solid composite electrolytes.

KEYWORDS: electrochemical reliability; lithium metal battery; lithium-ion transference number; double-layer solid composite electrolyte

Contents

Received December 30, 2023; accepted March 10, 2024

E-mails: 350926068@qq.com (Y.Q.), m15076477409@163.com (G.Y.)

∗ X.L., P.S., and L.L. contributed equally to this work.

1 Introduction

Given the increasing need for commercial energy storage solutions, researchers have directed significant attention towards lithium metal batteries (LMBs). This attention comes primarily from the high energy density capacity and exceptionally low reaction potential of the lithium metal, theoretically measured at 0 V versus Li^+/Li [1]. However, during operation, LMBs using an organic liquid electrolyte still suffer from safety risks resulting from the formation of lithium dendrites that can puncture through the diaphragm. Therefore, the development of LMBs with both high energy density and improved security is becoming increasingly important [2–3].

Generally, solid-state electrolytes are typically classified into three distinct categories: solid polymer electrolytes (SPEs), inorganic ceramic electrolytes (ICEs), and composite solid electrolytes (CSEs) [4]. Active inorganic electrolyte fillers, such as $Li_{0.33}La_{0.57}TiO_3$ (LLTO) [5–6], $Li_7La_3Zr_2O_{12}$ (LLZO) [7–8], $Li_{6.4}La_3Zr_{1.4}Ta_{0.6}O_{12}$ (LLZTO) [9–10], and $Li_{1.7}Al_{0.3}Ti_{1.7}(PO_3)_4$ (LATP) [11–12], are known to have a room-temperature ionic conductivity (σ) in the range of 10^{-5}–10^{-3} $S{\cdot}cm^{-1}$. Still, the cumbersome preparation process and poor electrode compatibility produce excellent interfacial resistance. In contrast, SPEs, including poly(ethylene oxide) (PEO) [13–14], poly(methyl methacrylate) (PMMA) [15–16], poly(acrylonitrile) (PAN) [17–18], and poly(propylene carbonate) (PPC) [19–20] with soft and pliable, are easy to be in close contact with the electrodes, but their development is hindered due to the low ionic conductance. CSEs not only overcome the problem of low conductivity of SPEs, but also alleviate the problem of increasing the interface resistance of batteries due to the contact difference of ICE surfaces [21–22]. By employing appropriate compositional modifications and suitable preparation techniques, CSEs can be tailored to exhibit specific properties. These include achieving the desired room-temperature σ value (1×10^{-4} $S{\cdot}cm^{-1}$), widening the electrochemical stability window (ESW), enhancing the lithium-ion transference number ($t(Li^+)$), and establishing favorable interfacial contacts [22]. However, the persistent challenge from the formation of lithium dendrites in solid-state LMBs still remains, causing inadequate cycling stability. Consequently, there is a need to engineer CSEs capable of effectively restraining the growth of lithium dendrite [23].

Constructing high-performance solid-state lithium metal batteries (SSLMBs) mandates a meticulous selection of materials. Yao and his colleagues [24] introduced an antioxidant poly(vinylidene fluoride-*co*-hexafluoropropylene)–10% LATP (PVDF–HFP–10% LATP) in contact with the cathode and PEO–5% LATP in contact with the anode, thereby producing a double-layer solid composite electrolyte (DLSCE). At room temperature, this DLSCE has the $t(Li^+)$ value of 0.43, the σ value of 1.49×10^{-4} $S{\cdot}cm^{-1}$, and the ESW of 4.82 V. Additionally, the DLSCE and the lithium metal anode were assembled in a Li/DLSCE/Li symmetric battery, maintaining stable operation for over 600 h at a current density of 0.2 $mA{\cdot}cm^{-2}$. This demonstrates excellent stability of the lithium metal and effective inhibition of the lithium dendrite formation. When assembled with a high-voltage $LiNi_{1/3}Co_{1/3}Mn_{1/3}O_2$ (NCM111) cathode, the Li/DLSCE/NCM111 cell showcases impressive electrochemical capabilities. Remarkably, it demonstrates prolonged cyclability with 85% capacity retention over 100 cycles at 0.2 C, maintaining a consistent 100% coulombic efficiency throughout. Wang and his colleagues [25] prepared a quasi-solid-state LMB containing the double-layer gel polymer electrolyte (GPE). The transitional layer, comprising PAN, PEO, and LATP, is positioned near the lithium anode to minimize side reactions of pure PAN. Also, in the meantime, the transition layer composed of PAN and LATP contacts with the cathode to improve the rate performance by exploiting the high σ value of PAN. The designed DLSCE has an enhanced $t(Li^+)$ value (0.55), with mechanical stress and stretch of 22.6 MPa and 180.4%, respectively.

In the present study, the ultraviolet (UV) curing technology was employed to fabricate a PVDF–HFP–PMMA/LLZTO double-layer polymer–inorganic composite solid electrolyte tailored for SSLMBs. PVDF–HFP is used in contact with the cathode due to its electrochemical stability at the oxidation potential and higher ionic conductivity, while PMMA is a structurally stable polymer matrix whose lithium metal stabilization is used as contact with the anode. It was found that this DLSCE possessed improved values of σ and $t(Li^+)$. Moreover, it demonstrates superior cycling performance, expanded ESW, and notably improved mechanical properties. Additionally, the DLSCE displays exceptional stability with the lithium metal, facilitating the stable operation of a Li/Li symmetric battery for over 200 h at

both 0.1 and 0.2 mA·cm^{-2}. Meanwhile, the resulted LFP/PEL–PMEL/Li battery exhibited remarkable current rate performance.

2 Materials and methods

2.1 Materials

The materials used in this study are as follows: N, N-dimethylformamide (DMF; Aladdin, China), $LiFePO_4$ (LFP; Macklin, China), super-P (SP; Shenzhen Kejing Star Technology Co., China), N-methyl-2-pyrrolidone (NMP; Aladdin, China), ethoxylated trimethylolpropane triacrylate (ETPTA; Sigma-Aldrich, China), 2-hydroxy-2-methylpropiophenone (HMPP; Ryoji, China), PVDF–HFP (Arkema, China), PVDF (Arkema, China), and lithium perchlorate ($LiClO_4$; Aladdin, China).

2.2 Preparation of PEL–PMEL

UV curing was utilized to fabricate the semi-interpenetrating polymer network (semi-IPN) film comprising PVDF–HFP, and the synthesis procedure is depicted in Fig. 1. Initially, 2 g PVDF–HFP was dissolved in the DMF solution, followed by the addition of LLZTO and $LiClO_4$ to stir the electrolyte membrane for 12 h with the temperature set at 60 °C. Then, ETPTA and the photoinitiator HMPP were mixed and stirred for 5 min to obtain Solution I. The electrolyte membrane obtained after curing of Solution I is called PEL, which was in contact with the positive electrode. The steps for preparing the electrolyte membrane in contact with the negative electrode were the same as those described above, except that the polymer PVDF–HFP in Solution I was replaced with PMMA, while other components remained unchanged, thus forming Solution II. The electrolyte membrane obtained after curing of Solution II is called PMEL. Solution I was poured onto a polytetrafluoroethylene (PTFE) plate, UV-cured under an UV lamp (Lichtzen) at a peak irradiation intensity of 1200 MW·cm^{-2} for 60 s, and vacuum-dried in an oven at 60 °C for 4 h to obtain the transition layer of the PEL electrolyte membrane. Subsequently, Solution II was poured onto PEL to prepare the PMEL layer using the

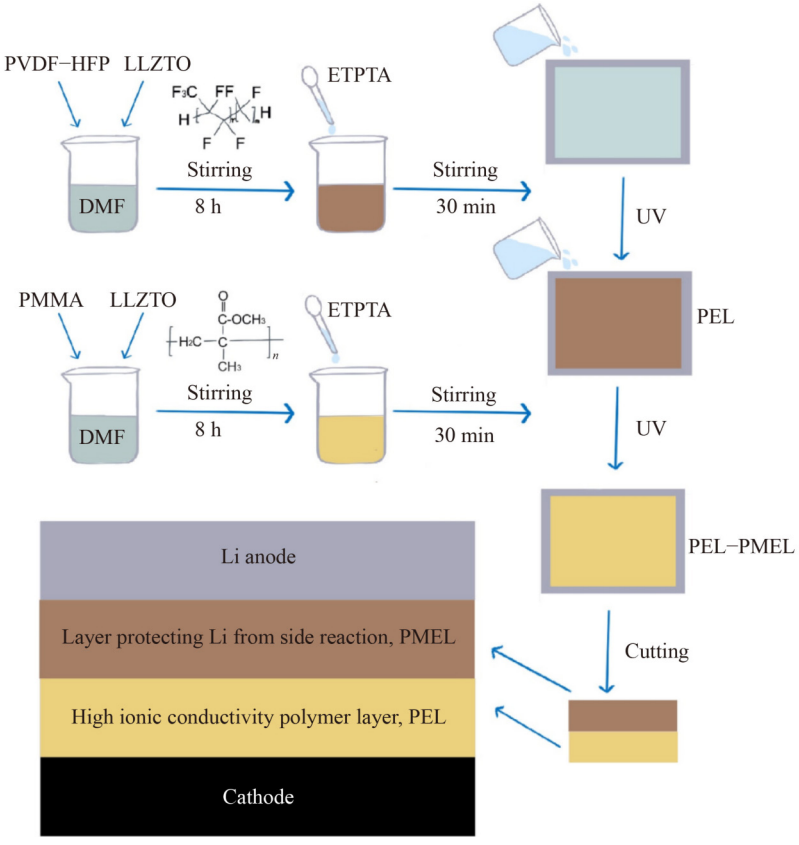

Fig. 1 Preparation process of the PEL–PMEL electrolyte.

same process as described above. Afterwards, the double-layer electrolyte membrane, PEL–PMEL, was dried in the vacuum oven at 60 °C for 12 h, followed by shaping into discs (19 mm in diameter) and collecting in a glove box. Figure 1 illustrates the working mechanism and the stacking model of the PEL–PMEL electrolyte in a solid-state battery, showcasing how such two distinct layers function electrochemically.

2.3 Preparation of LLZTO

LLZTO was prepared through a solid-phase reaction method presented in Ref. [26]. $LiOH{\cdot}H_2O$, La_2O_3, ZrO_2, Al_2O_3, and Ta_2O_5 were firstly dissolved in isopropyl alcohol (IPA; Aladdin) and stirred through a magnetic stirrer for 8 h, following which the uniform solution was placed at 80 °C for solvent evaporation. Subsequently, the obtained slurry was annealed at 900 °C for 6 h. After mechanical grinding (MG) with isopropanol as the milling medium using a planetary ball-milling machine (QM-3SP4; Nanda Instrument Co., Ltd.) at 280 $r{\cdot}min^{-1}$ for 13 h, the resulted slurry was filtered, dried in a vacuum oven, and finally stored in a glove box.

2.4 Structural characterization

Scanning electron microscopy (SEM) was performed to examine the surface morphology of samples through a Tescan MIRA instrument (Brno, Czech Republic). X-ray diffraction (XRD) was carried out on a DX-2700 X-ray diffractometer (Dandong, China) using Cu Kα radiation operated at 30 kV and 40 mA to determine the internal crystal structures of materials. Thermogravimetric analysis (TGA) results were obtained using the PerkinElmer STA 8000 instrument with the heating rate of 10 $°C{\cdot}min^{-1}$, the testing temperature range of 20–800 °C, and the protective atmosphere of nitrogen (N_2). Stress chain tests were performed on an Instron 5982 material testing machine at a crosshead speed of 20 $mm{\cdot}min^{-1}$.

2.5 Electrochemical testing

To prepare the $LiFePO_4$ cathode, 80% LFP, 10% PVDF, and 10% conductive carbon were added in the NMP solvent, and the obtained solution was stirred for 6 h, following which the resulted slurry was evenly spread onto the aluminum foil. Afterwards, the aluminum foil coated with the positive electrode solution was vacuum-dried at 80 °C for 36 h, and the obtained sample was cut into positive electrode circles 14 mm in diameter, with the mass of the $LiFePO_4$ cathode active substance ranging from 2.5 to 3 mg. The assembled LFP/PEL–PMEL/Li battery was then subjected to the electrochemical testing in a voltage range of 2.8–4.0 V. The electrolyte membrane was immersed in a liquid electrolyte (1.0 $mol{\cdot}L^{-1}$ $LiPF_6$ in ethylene carbonate (EC):dimethyl carbonate (DMC):ethylmethyl carbonate (EMC) (1:1:1, v/v/v) with 1.0% lithium difluoro(oxalato)borate (LiDFOB)) for 12 h to fully infiltrate PEL–PMEL and improve the interface compatibility with the electrode.

The assembly of the CR2025 button cell involved incorporating the $LiFePO_4$ cathode, the lithium anode, and the PEL–PMEL electrolyte within a glove box maintained under an argon atmosphere ($c(H_2O)$ < 5 ppm and $c(O_2)$ < 5 ppm (1 ppm = 10^{-6})).

Cyclic voltammetry (CV) was carried out using the DH7000 electrochemical workstation at a scan rate of 0.1 $mV{\cdot}s^{-1}$ between 2.8 and 4 V. The impedance of PEL–PMEL was measured by assembling stainless steel (SS) and PEL–PMEL into SS/PEL–PMEL/SS (frequency: 10^6 Hz–0.01 Hz; alternative current (AC) voltage amplitude: 10 mV). The ionic conductivity, σ ($S{\cdot}cm^{-1}$), can thus be calculated based on Eq. (1) as follows:

$$\sigma = \frac{L}{RS} \tag{1}$$

where L is the thickness (cm) of the membrane, R is the bulk resistance (Ω) of the electrolyte, and S is the contact area (0.64 cm^2) between the membrane and the SS.

Using the symmetric battery made of Li/double-layer solid electrolyte/Li, and jointly conducting both electrochemical impedance spectroscopy (EIS) and direct current (DC) polarization measurements on the same electrochemical station, the transference number of lithium ions, $t(Li^+)$, can be calculated according to Eq. (2) as follows:

$$t(Li^+) = \frac{I_s(\Delta V - R_0 I_0)}{I_0(\Delta V - R_s I_s)} \tag{2}$$

where ΔV is the step voltage, I_0 and I_s are the initial- and steady-state currents, respectively, while R_0 and R_s are the initial- and steady-state resistances, respectively.

Battery charging and discharging characterizations, cycling tests, and rate capability assessments were performed at room temperature using a Neware battery

tester covering a voltage range from 2.8 to 4 V.

3 Results and discussion

The trivalent ethylene group within ETPTA offers a promising avenue for UV curing owing to its high curing activity and high curing efficiency, also potentially serving as a mechanical framework within the system. In this process, the introduction of ETPTA, a macromonomer, with PVDF–HFP and PMMA initiates the polymerization process under UV-light irradiation, resulting in the formation of a network structure that collectively constitutes an electrolyte with semi-IPN fabric. Given the potential impact of an excess of ETPTA on the electrolyte conductivity, various electrolyte membranes were prepared with different weight ratios of PVDF–HFP/ETPTA (1:1, 2:1, 3:1, 4:1) and PMMA/ETPTA (1:1, 2:1, 3:1, 4:1). According to EIS results of PEL shown in Fig. 2(a), the measured resistances of samples are 643, 525, 342, and 354 Ω, while according to those of PMEL exhibited in Fig. 2(c), the sample resistances are measured to be 344, 206, 180, and 228 Ω, separately. A notable observation is that the

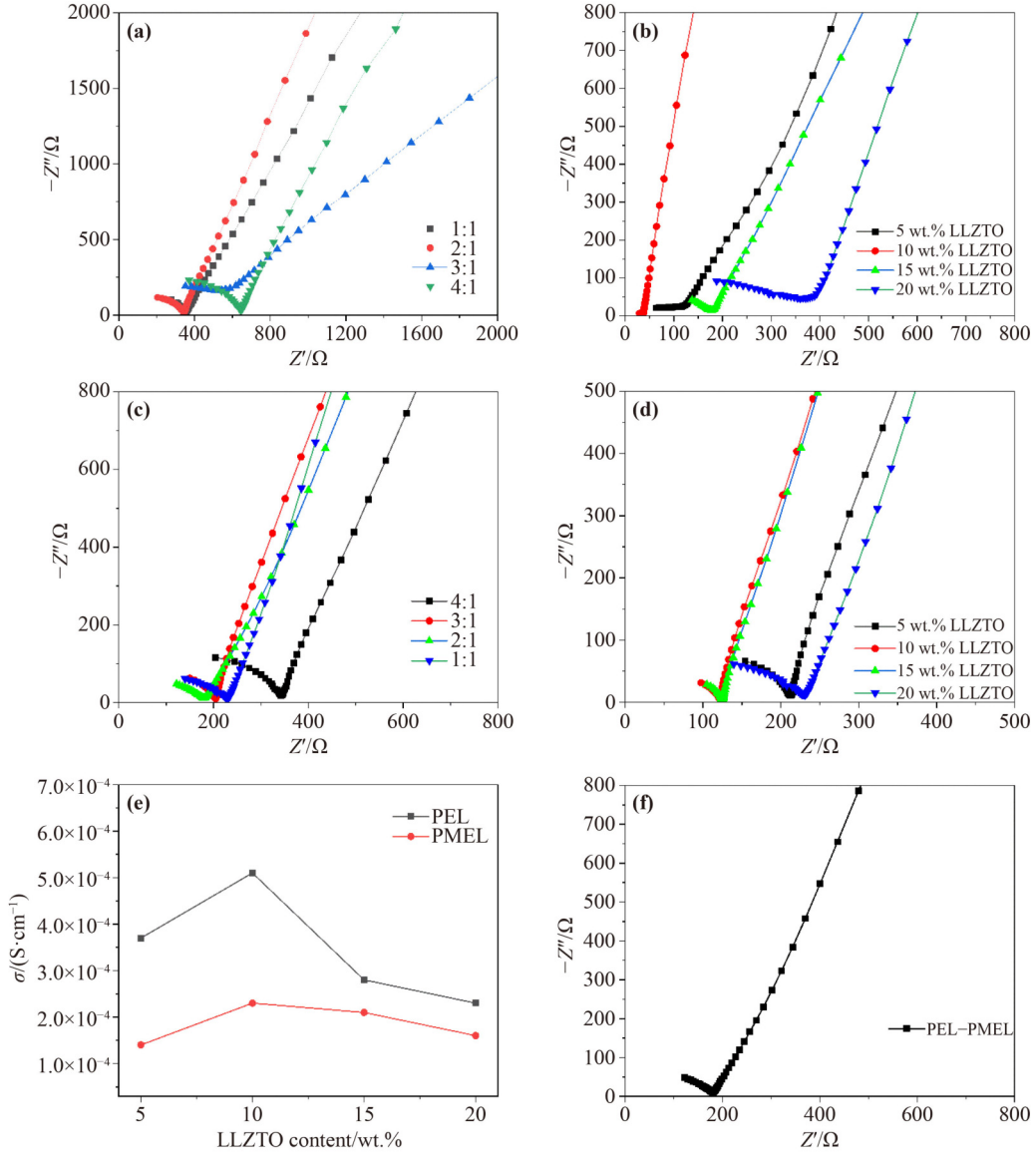

Fig. 2 EIS curves of PEL with (**a**) different weight ratios of PVDF–HFP/ETPTA and (**b**) different weight contents of LLZTO. EIS curves of PMEL with (**c**) different weight ratios of PMMA/ETPTA and (**d**) different weight contents of LLZTO. (**e**) Variation of σ values of PEL and PMEL with the weight content of LLZTO. (**f**) EIS result of PEL–PMEL.

resistances of such two series reach the minimum values when the weight ratios of both PVDF–HFP:ETPTA and PMMA:ETPTA are 2:1. With further enhancing the content of ETPTA, the resistance shows an upward trend. This observation can be attributed to the internal molecular agglomeration of excessive ETPTA, resulting in the resistance increase of the electrolyte membrane [27].

Meanwhile, introducing LLZTO into the electrolyte membrane is beneficial as inorganic fillers can effectively enhance the crystallinity of polymers and augment the transference channel of lithium ions, consequently improving both the mechanical property and the ionic conductivity of the electrolyte membrane. However, excessive addition of LLZTO may lead to loss of flexibility and accumulation of LLZTO packings, reducing the σ value of the electrolyte film. Because the content of CSEs has influence on the σ value of the electrolyte membrane, CSEs with four different contents of LLZTO were prepared for comparison. As shown in Figs. 2(b) and 2(d), with the increase of the LLZTO content, the σ value of the electrolyte membrane increases at first. When the LLZTO content is equal to 10 wt.%, the σ value of PEL-10 wt.% is 2.3×10^{-4} S·cm^{-1}, while that of PMEL-10 wt.% reaches 5.1×10^{-4} S·cm^{-1}. With continued enhancement of the LLZTO content, the σ values for both series of PEL and PMEL decrease (Fig. 2(e)). Therefore, the LLZTO content of 10 wt.% is selected for either PEL or PMEL in the following study. It can be seen from Fig. 2(f) that the R value of PEL–PMEL is 121 Ω, while the σ value is 2.6×10^{-4} S·cm^{-1} as calculated based on Eq. (1).

In Fig. 3(a), characteristic peaks at the 2θ values of 18°, 20°, and 40° are observable for PVDF–HFP. After the UV photofixation, the peaks at 18° and 20° are notably altered, with the overall peak shape broadened, signifying that the polymerization of the ETPTA macromonomer within PVDF–HFP diminishes its overall crystallinity [28]. The appearance of characteristic LLZTO peaks for the pattern of PEL suggests the successful doping of LLZTO nanoparticles (NPs) into PVDF–HFP. In addition, the diffraction intensity of the peak at 18°–20° for PEL is lower than that for PVDF–HFP, indicating that the addition of LLZTO reduces the crystallinity of PVDF–HFP and expands the amorphous region [29]. The XRD patterns of PMMA, ETPTA, LLZTO, and PMEL

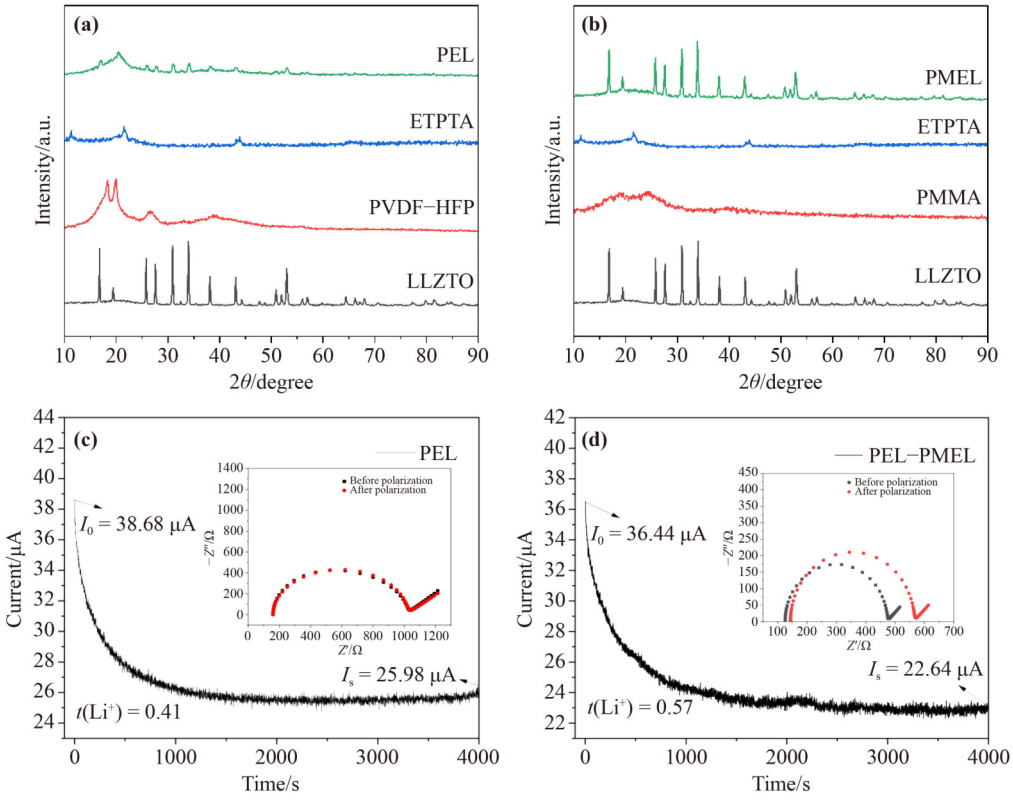

Fig. 3 XRD patterns: (**a**) PEL, ETPTA, PVDF–HFP, and LLZTO; (**b**) PMEL, ETPTA, PMMA, and LLZTO. Chronoamperometry profiles with AC impedance spectra (inset) of (**c**) PEL and (**d**) PEL–PMEL.

are shown in Fig. 3(b). PMMA is a long-chain molecular compound that exhibits an irregular internal arrangement with no distinct characteristic peaks. The hump of PMEL was further reduced by the addition of ETPTA and LLZTO, and all the characteristic peaks of LLZTO likewise appeared in the spectrum of PMEL.

The $t(Li^+)$ value is also one of the critical parameters for evaluating the performance of SSLMBs. The measurement results of PEL and PEL–PMEL obtained by assembling Li/Li symmetric batteries with timed polarization current curves and AC impedance spectra before and after the polarization (inset) are shown in Figs. 3(c) and 3(d), respectively. The $t(Li^+)$ value of PEL–PMEL is found to be 0.57, significantly higher than that of PEL (0.41). The significant increase of $t(Li^+)$ can be attributed to the interaction between LLZTO ceramic powders and polymers, which facilitates the relaxation of polymer chains, accelerates the movement of chain segments, and promotes the transference of lithium ions. Previous research has also revealed that the addition of the inorganic filler LLZTO can effectively enhance the mechanical properties of the main body, increase the transmission mode and transmission channel of Li^+, and reduce the crystallinity of the polymer, thus enhancing the Li^+ conduction [30–31].

Figure 4 presents both surface and cross-sectional microscopic morphologies of the electrolyte membrane. From Figs. 4(a) and 4(b), it is apparent that PMEL has a smoother and more compact surface compared to that of PEL. This characteristic of PMEL facilitates improved interface contact between the electrolyte and the electrode [32]. However, differing from what is observed on that of the PMMA-based electrolyte, there are LLZTO particles attached on the surface of the PVDF–HFP-based electrolyte, which can be associated with extended desiccation during the preparation process, resulting in the precipitation of LLZTO.

The investigation into the specific binding of two electrolytes within the battery was conducted by analyzing the cross-section of PEL–PMEL. As depicted in Fig. 4(c), there is a tight binding between both electrolytes, showcasing clear boundaries without any gaps, thereby indicating their compatibility. The elemental distributions of the double-layer electrolyte membrane can be visualized through the energy-dispersive spectroscopy (EDS) elemental analysis. Since PMMA does not contain F while PVDF–HFP does, no F is in contact with the anode while there is F on the side of the cathode, clearly presented in Fig. 4(d). Meanwhile, from Figs. 4(e) and 4(f), it is deduced that the elements of Ta and Zr are evenly distributed in the junction area between solid electrolytes.

The stability relationship between the solid electrolyte membrane and the lithium anode was investigated by means of the lithium plating/stripping test. Li/Li symmetric batteries using the PEL monolayer membrane and the PEL–PMEL bilayer membrane as solid electrolytes were assembled and charged/discharged at 0.1 and 0.2 $mA \cdot cm^{-2}$ to test their dendrite inhibition, with the testing results revealed in Figs. 5(a) and 5(b), respectively. At a set current density, both PEL and PEL–PMEL exhibited stable lithium plating/stripping processes, cycling for 100 h at 0.1 and 0.2 $mA \cdot cm^{-2}$. The LFP/PEL–PMEL/Li battery showed a very stable polarization

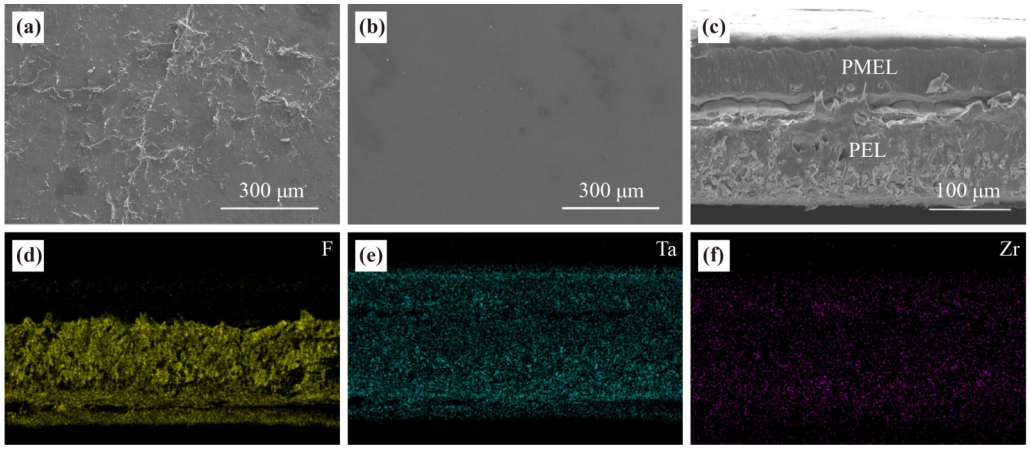

Fig. 4 SEM images of (**a**) PEL, (**b**) PMEL, and (**c**) the cross-section of PEL–PMEL. Element mapping images of the PEL section: (**d**) F; (**e**) Ta; (**f**) Zr.

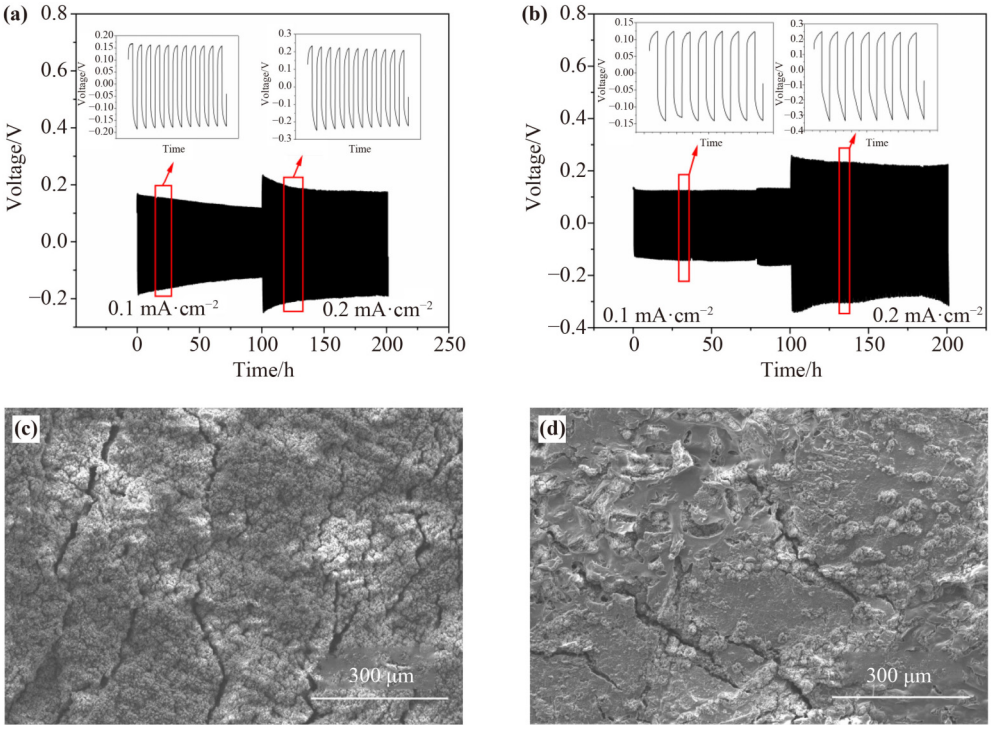

Fig. 5 Rate performances of Li/Li symmetric batteries assembled using different solid electrolytes under 0.1 and 0.2 mA·cm^{-2}: (**a**) the PEL monolayer; (**b**) the PEL–PMEL bilayer. SEM images of lithium-sheet surfaces in contact with (**c**) the PEL layer and (**d**) the PEL–PMEL layer used as solid electrolytes in assembled batteries after cycling for 200 h.

voltage during the 200 h cycling, but the polarization voltage of PEL–PMEL was significantly lower than that of PEL at 0.16 V and 0.1 mA·cm^{-2}. The results show a better lithium plating/stripping process for PEL–PMEL, proving that PEL–PMEL forms a more stable and uniform solid electrolyte interphase (SEI) membrane with the lithium anode after a period of circulation. As shown in Figs. 5(c) and 5(d), the surface of the lithium sheet in contact with the PEL layer is relatively rough, while that with the PEL–PMEL layer is relatively smooth after cycling for 200 h. It shows that the side reaction between the PEL–PMEL layer and the anode lithium sheet is minor, which makes the interface stability of lithium coating performance and stripping performance more stable [33].

The thermal stability of solid-state electrolyte membranes plays a pivotal role in ensuring the safety of solid-state batteries. Figure 6(a) comparatively shows TGA curves of both the PEL monolayer membrane and the PEL–PMEL bilayer membrane. The curves indicate that both CSE membranes exhibited a slight weight loss when the temperature rose up to 200 °C, likely due to the evaporation of residual solvents and water within the electrolyte membrane. With the further increase of the temperature, PEL started to deteriorate at 350 °C due to the decomposition of the polymer network formed through the polymerization of ETPTA [34–35], while the PVDF–HFP matrix decomposed at around 425 °C. For the PEL–PMEL bilayer, although the PMMA decomposition temperature was around 270 °C, the weight loss actually started early at 220 °C owing to the destruction of the cross-linking between ETPTA and PMMA. As the temperature rose continuously, PVDF–HFP decomposed. At 800 °C, the weight loss rates of PEL and PEL–PMEL reached 89.84% and 81.11%, respectively, indicating that PEL–PMEL maintains more weight, a factor positively enhancing the thermal stability of the CSE. Currently, excellent mechanical properties are among the most essential features for diaphragms to gain commercial applications.

The mechanical properties of PVDF–HFP/ETPTA, PEL, and PEL–PMEL electrolyte membranes were investigated through tensile strength tests. From Fig. 6(b), it is seen that the maximum mechanical tension stress and strain are 10.3 MPa and 300.9% for PVDF–HFP/ETPTA while 16.1 MPa and 195.5% for PEL, respectively. As for PEL–PMEL, such two values reach 17.8 MPa and 88.1%, respectively, implying good strength and stiffness of this

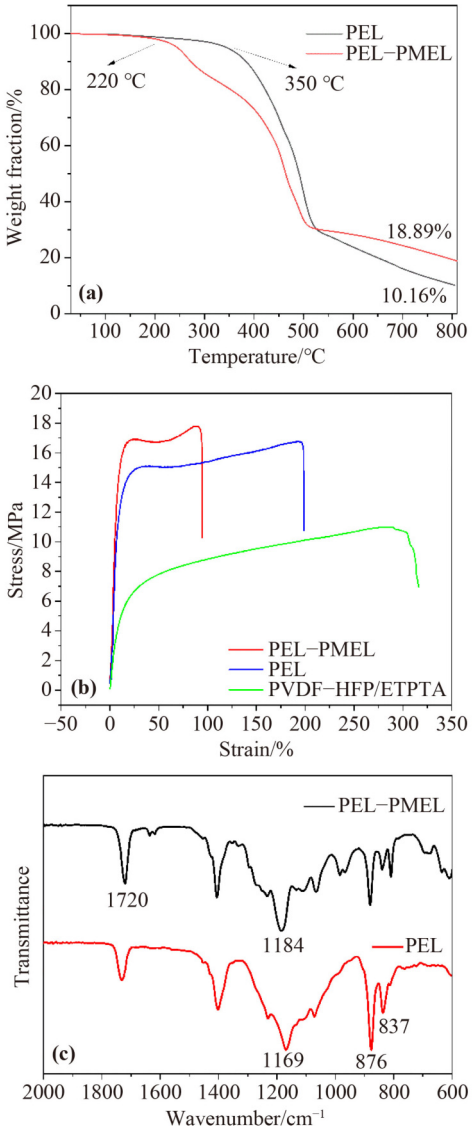

Fig. 6 (**a**) TGA curves of PEL and PEL–PMEL electrolyte membranes. (**b**) Stress–strain curves of PVDF–HFP/ETPTA, PEL, and PEL–PMEL electrolyte membranes. (**c**) FTIR spectra of PEL and PEL–PMEL electrolyte membranes.

electrolyte membrane. Compared with those of PEL, the elastic modulus and the maximum stress of the PEL–PMEL electrolyte membrane rise when the strain decreases. This enhancement is attributed to the superior mechanical strength deriving from the inherent multilayer structure of the solid electrolyte, which ensures long cycling of solid lib without mechanical failure, thereby improving the safety [36]. Figure 6(c) presents FTIR spectra of PEL and PMEL membranes, which can help analyze their chemical compositions. It is detected that there are expansion peaks located at 837, 876, and 1169 cm^{-1}, which are attributed to the vibrations of C−F and C−F_3 for PVDF–HFP, respectively. At the same time, the intense sharp peak at about 1720 cm^{-1} is ascribed to the carbonyl stretching of the pendent group −($COOCH_3$), while the distinct band at 1169 cm^{-1} to a distortion of CH_3 [37].

Figure 7(a) illustrates performance comparison between the LFP/PEL/Li battery and the LFP/PEL–PMEL/Li battery at various current rates ranging from 0.1 to 1 C. At room temperature, the assembled LFP/PEL/Li and LFP/PEL–PMEL/Li batteries exhibit discharge specific capacities of 132.9 and 162.4 $mA{\cdot}h{\cdot}g^{-1}$, respectively, when operated at a current density of 0.1 C. It is seen that the LFP/PEL–PMEL/Li battery demonstrates relatively higher discharge specific capacities compared to those of the LFP/PEL/Li battery corresponding to the same current rate, particularly at higher current rates. Crucially, upon the return to the current rate of 0.1 C, the LFP/PEL/Li battery retains a discharge specific capacity of only 113.6 $mA{\cdot}h{\cdot}g^{-1}$, while the LFP/PEL–PMEL/Li battery maintains a high value of 161.9 $mA{\cdot}h{\cdot}g^{-1}$, which is close to the initial one. At the same time, PEL–PMEL maintains almost 99% coulombic efficiency during charging and discharging, suggesting that the PEL–PMEL electrolyte membrane has structural and electrochemical stability and good capacity reversibility. The initial charge–discharge curves of the LFP/PEL–PMEL/Li battery at various current rates are depicted in Fig. 7(b). These curves reveal discharge specific capacities of 162.4, 146.9, 93.6, and 64.0 $mA{\cdot}h{\cdot}g^{-1}$ at 0.1, 0.2, 0.5, and 1 C, respectively. With an increase of the charge–discharge rate, the polarization is inevitably intensified, resulting in the decline of the charge–discharge specific capacity.

Figure 7(c) shows cycling performances of LFP/PEL/Li and LFP/PEL–PMEL/Li batteries under 0.5 C at room temperature. It can be seen that the initial discharge specific capacities of LFP/PEL/Li and LFP/PEL–PMEL/Li are 60.2 and 93.0 $mA{\cdot}h{\cdot}g^{-1}$, respectively. After 50 cycles, the discharge specific capacities of LFP/PEL/Li and LFP/PEL–PMEL/Li are 54.0 and 81.4 $mA{\cdot}h{\cdot}g^{-1}$, and the corresponding retention rates are 89.7% and 87.5%, respectively. Moreover, their coulombic efficiencies remain above 99% after charging and discharging for 50 cycles. Although the retention rates of such two batteries are close to each other, the battery assembled with the double-layer electrolyte membrane has higher discharge specific capacity, and its discharge specific capacity curve is also smoother than that of LFP/PEL/Li, because PVDF–HFP has more side reactions with the lithium

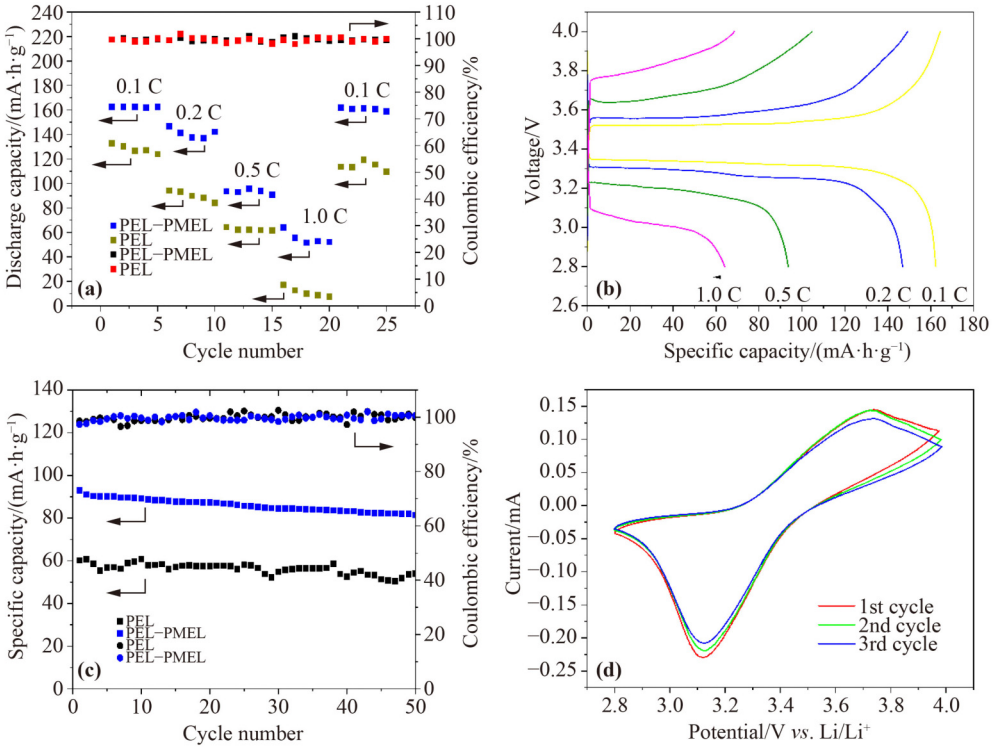

Fig. 7 Electrochemical performances of solid-state batteries: (**a**) rate capabilities of 0.1, 0.2, 0.5, and 1 C for LFP/PEL/Li and LFP/PEL–PMEL/Li batteries; (**b**) voltage–specific capacity curves at different rates for the LFP/PEL–PMEL/Li battery; (**c**) cycling performances of LFP/PEL/Li and LFP/PEL–PMEL/Li batteries under 0.5 C; (**d**) CV curves of the PEL–PMEL electrolyte membrane corresponding to the cycling at different turns.

metal, resulting in the uneven deposition of Li_2O on the surface of lithium metal and the formation of dead lithium, whereas PMMA has a stable structure stabilizing the lithium metal, and the formation of the passivation film in contact with the electrode surface can lead to less resistance. Incorporating the PMMA layer enhances the interfacial contact between the electrolyte membrane and the negative electrode, thereby significantly improving the cycling stability of the battery [38]. Figure 7(d) shows CV curves of the LFP/PEL–PMEL/Li battery corresponding to different cycles in the potential range of 2.8–4 V at a scan rate of 0.5 $mV \cdot s^{-1}$. It demonstrates that this battery has a clear reduction peak at ~3.1 V and a strong oxidation peak at ~3.7 V, corresponding to the stripping of lithium ions from LFP. The basic overlap of CV curves of the first three cycles verifies good electrochemical reversibility of the PEL–PMEL electrolyte membrane used in this battery.

4 Conclusions

In conclusion, to address challenges in the low σ value of electrolytes and high resistance across electrode–electrolyte interfaces faced by commercial applications of SSLMBs, a novel double-layer electrolyte has been successfully prepared by UV curing process to enhance the electrochemical properties of SSLMBs. The PVDF–HFP/PMMA polymer-based DLSCE exhibits high σ value, and its application in the LFP/PEL–PMEL/Li battery effectively improves the interfacial compatibility as well as the chemical and electrochemical stability between the electrolyte and the electrode. The results show that σ, $t(Li^+)$, and the tensile strength of PEL–PMEL are 2.6×10^{-4} $S \cdot cm^{-1}$, 0.57, and 17.8 MPa, respectively. In addition, the battery assembled with PEL–PMEL has good electrochemical performance and cycling stability. At a current density of 0.1 C, the initial discharge specific capacity was 162.4 $mA \cdot h \cdot g^{-1}$, and after high current discharging (0.1–1 C), it remained at 161.9 $mA \cdot h \cdot g^{-1}$ at 0.1 C. At 0.5 C, the initial discharge specific capacity of Li/PEL–PMEL/Li was 93.0 $mA \cdot h \cdot g^{-1}$, and after 50 cycles, it maintained at 81.4 $mA \cdot h \cdot g^{-1}$, with the capacity retention rate of 89.7%. This work presents a cost-effective and efficient approach to designing new electrolytes that have promising

prospects for the commercialization of LMBs in the new energy sector.

Authors' contributions Conceptualization, X.L. and P.S.; methodology, J.W.; software, P.S.; validation, X.L., P.S. and G.Y.; formal analysis, M.H. and Y.W.; investigation, P.S. and Q.H; resources, X.L.; data curation, P.S.; writing — original draft preparation, P.S.; writing — review and editing, X.L.; visualization, L.L.; supervision, X.L.; project administration, X.L.; funding acquisition, L.L. All authors have read and agreed to the published version of the manuscript.

Declaration of competing interests The authors declare that they have no competing interests.

Acknowledgements This research was supported by the Liuzhou Science and Technology Fund Project (Grant No. 2023PRj0103), the National Natural Science Foundation of China (Grant Nos. 52161033 and 22262005), the Guangxi Key Laboratory of Automobile Components and Vehicle Technology Fund Project (Grant Nos. 2022GKLACVTKF02 and 2023GKLACVTZZ02), and the Fund Project of the Key Lab of Guangdong Science and Technology Innovation Strategy Special Fund Project in 2023 (Grant No. pdjh2023a0819).

References

[1] Hung I M, Mohanty D. Preparation and characterization of LLZO–LATP composite solid electrolyte for solid-state lithium-ion battery. Solid State Communications, 2023, 364: 115135

[2] Chen Z, Kim G T, Kim J K, et al. Highly stable quasi-solid-state lithium metal batteries: reinforced $Li_{1.3}Al_{0.3}Ti_{1.7}(PO_4)_3$/Li interface by a protection interlayer. Advanced Energy Materials, 2021, 11(30): 2101339

[3] Liang X, Ning Y, Lan L, et al. Electrochemical performance of a PVDF–HFP–$LiClO_4$–$Li_{6.4}La_3Zr_{1.4}Ta_{0.6}O_{12}$ composite solid electrolyte at different temperatures. Nanomaterials, 2022, 12(19): 3390

[4] Zhang W J, Li S L, Zhang Y R, et al. A quasi-solid-state electrolyte with high ionic conductivity for stable lithium-ion batteries. Science China: Technological Sciences, 2022, 65(10): 2369–2379

[5] Cho Y H, Wolfenstine J, Rangasamy E, et al. Mechanical properties of the solid Li-ion conducting electrolyte: $Li_{0.33}La_{0.57}TiO_3$. Journal of Materials Science, 2012, 47(16): 5970–5977

[6] Liu S, Zhao Y, Li X, et al. Solid-state lithium metal batteries with extended cycling enabled by dynamic adaptive solid-state interfaces. Advanced Materials, 2021, 33(12): 2008084

[7] Ping X, Zheng Q, Meng B, et al. Influence of sintering atmosphere on the phase, microstructure, and lithium-ion conductivity of the Al-doped $Li_7La_3Zr_2O_{12}$ solid electrolyte. Ceramics International, 2022, 48(18): 25689–25695

[8] Su J, Huang X, Song Z, et al. Overcoming the abnormal grain growth in Ga-doped $Li_7La_3Zr_2O_{12}$ to enhance the electrochemical stability against Li metal. Ceramics International, 2019, 45(12): 14991–14996

[9] Ren Y, Shen Y, Lin Y, et al. Direct observation of lithium dendrites inside garnet-type lithium-ion solid electrolyte. Electrochemistry Communications, 2015, 57: 27–30

[10] Han F, Westover A S, Yue J, et al. High electronic conductivity as the origin of lithium dendrite formation within solid electrolytes. Nature Energy, 2019, 4(3): 187–196

[11] Liang Y, Lin Z, Qiu Y, et al. Fabrication and characterization of LATP/PAN composite fiber-based lithium-ion battery separators. Electrochimica Acta, 2011, 56(18): 6474–6480

[12] Lu X, Hai J, Zhang F, et al. Preparation and infiltration of NASICON-type solid electrolytes with microporous channels. Ceramics International, 2022, 48(2): 2203–2211

[13] Nam M G, Moon J, Kim M, et al. p‐Phenylenediamine-bridged binder-electrolyte-unified supramolecules for versatile lithium secondary batteries. Advanced Materials, 2024, 36(5): 2304803

[14] Xu L, Xiao X, Tu H, et al. Engineering functionalized 2D metal–organic frameworks nanosheets with fast Li^+ conduction for advanced solid li batteries. Advanced Materials, 2023, 35(38): 2303193

[15] Hu J H. Mechanical and optical properties of PMMA prepared by modified microemulsion polymerization. Acta Chimica Sinica, 2009, 6712: 1370

[16] Ooe M, Miyata K, Yoshioka J, et al. Direct observation of mobility of thin polymer layers via asymmetric interdiffusion using neutron reflectivity measurements. The Journal of Chemical Physics, 2019, 151(24): 244905

[17] Han Z, Dong Y, Liu C. Coordination of modified PAN fibers with Fe^{3+} and catalytic activity of their complexes for dye degradation. Chemical Journal of Chinese Universities, 2010, 315: 986–993

[18] Wu Q Y, Chen X N, Wan L S, et al. Interactions between polyacrylonitrile and solvents: density functional theory study and two-dimensional infrared correlation analysis. The Journal of Physical Chemistry B, 2012, 116(28): 8321–8330

[19] Cui S, Li L, Wang Q. Fabrication of (PPC/NCC)/PVA composites with inner-outer double constrained structure and improved glass transition temperature. Carbohydrate Polymers, 2018, 191: 35–43

[20] Ullrich C K, Lehmann L, London W B, et al. End-of-life care patterns associated with pediatric palliative care among children who underwent hematopoietic stem cell transplant. Biology of Blood and Marrow Transplantation, 2016, 22(6): 1049–1055

[21] Dirican M, Yan C, Zhu P, et al. Composite solid electrolytes for all-solid-state lithium batteries. Materials Science and Engineering R: Reports, 2019, 136: 27–46

[22] Huang Y, Zhang Z, Gao H, et al. $Li_{1.5}Al_{0.5}Ti_{1.5}(PO_4)_3$ enhanced polyethylene oxide polymer electrolyte for all-solid-state lithium batteries. Solid State Ionics, 2020, 356: 115437

[23] Barai P, Higa K, Srinivasan V. Lithium dendrite growth mechanisms in polymer electrolytes and prevention strategies. Physical Chemistry Chemical Physics, 2017, 19(31): 20493–20505

[24] Yao Z, Zhu K, Li X, et al. Double-layered multifunctional composite electrolytes for high-voltage solid-state lithium–metal batteries. ACS Applied Materials & Interfaces, 2021, 13(10): 11958–11967

[25] Wang X, Hao X, Xia Y, et al. A polyacrylonitrile (PAN)-based double-layer multifunctional gel polymer electrolyte for lithium–sulfur batteries. Journal of Membrane Science, 2019, 582: 37–47

[26] He T, Zeng G, Feng C, et al. A solid-electrolyte-reinforced separator through single-step electrophoretic assembly for safe high-capacity lithium ion batteries. Journal of Power Sources, 2020, 448: 227469

[27] Xie H X, Fu Q G, Li Z, et al. Ultraviolet-cured semi-interpenetrating network polymer electrolytes for high-performance quasi-solid-state lithium metal batteries. Chemistry, 2021, 27(28): 7773–7780

[28] Liu L, Wang X, Yang C, et al. PVDF–HFP-based gel polymer electrolyte with semi-interpenetrating networks for dendrite-free lithium metal battery. Acta Metallurgica Sinica: English Letters, 2021, 34(3): 417–424

[29] Wang D, Cai D, Zhong Y, et al. A three-dimensional electrospun $Li_{6.4}La_3Zr_{1.4}Ta_{0.6}O_{12}$–poly (vinylidene fluoride-hexafluoro-propylene) gel polymer electrolyte for rechargeable solid-state lithium ion batteries. Frontiers in Chemistry, 2021, 9: 751476

[30] Gu Y, Liu H. PVDF–HFP/LLZTO composite electrolytes with UV cure for solid-state lithium rechargeable batteries. Journal of Solid State Electrochemistry, 2023, 27(10): 2671–2679

[31] Li S, Zhang S Q, Shen L, et al. Progress and perspective of ceramic/polymer composite solid electrolytes for lithium batteries. Advanced Science, 2020, 7(5): 1903088

[32] Li S, Lu J, Geng Z, et al. Solid polymer electrolyte reinforced with a $Li_{1.3}Al_{0.3}Ti_{1.7}(PO_4)_3$-coated separator for all-solid-state lithium batteries. ACS Applied Materials & Interfaces, 2022, 14(1): 1195–1202

[33] Zheng X, Liu K, Yang T, et al. Sandwich composite PEO@$(Er_{0.5}Nb_{0.5})_{0.05}Ti_{0.95}O_2$@cellulose electrolyte with high cycling stability for all-solid-state lithium metal batteries. Journal of Alloys and Compounds, 2021, 877: 160307

[34] Fan H, Yang C, Wang X, et al. UV-curable PVDF–HFP-based gel electrolytes with semi-interpenetrating polymer network for dendrite-free lithium metal batteries. Journal of Electroanalytical Chemistry, 2020, 871: 114308

[35] Luo K, Shao D, Yang L, et al. Semi-interpenetrating gel polymer electrolyte based on PVDF–HFP for lithium ion batteries. Journal of Applied Polymer Science, 2021, 138(11): e49993

[36] Xu K, Xu C, Jiang Y, et al. Sandwich structured PVDF–HFP-based composite solid electrolytes for solid-state lithium metal batteries. Ionics, 2022, 28(7): 3243–3253

[37] Yousefi F, Mousavi S B, Heris S Z, et al. UV-shielding properties of a cost-effective hybrid PMMA-based thin film coatings using TiO_2 and ZnO nanoparticles: a comprehensive evaluation. Scientific Reports, 2023, 13(1): 7116

[38] Zhang J, Chen S, Xie X, et al. Porous poly(vinylidene fluoride-co-hexafluoropropylene) polymer membrane with sandwich-like architecture for highly safe lithium ion batteries. Journal of Membrane Science, 2014, 472: 133–140